

# Next-generation *in vivo* optical imaging with short-wave infrared quantum dots

Oliver T. Bruns<sup>1‡\*</sup>, Thomas S. Bischof<sup>1‡\*</sup>, Daniel K. Harris<sup>1,2</sup>, Daniel Franke<sup>1</sup>, Yanxiang Shi<sup>3</sup>, Lars Riedemann<sup>4‡</sup>, Alexander Bartelt<sup>5</sup>, Frank B. Jaworski<sup>6</sup>, Jessica A. Carr<sup>1</sup>, Christopher J. Rowlands<sup>7</sup>, Mark W. B. Wilson<sup>1‡</sup>, Ou Chen<sup>1‡</sup>, He Wei<sup>1</sup>, Gyu Weon Hwang<sup>1,2‡</sup>, Daniel M. Montana<sup>1,2</sup>, Igor Coropceanu<sup>1</sup>, Odin B. Achorn<sup>1</sup>, Jonas Kloepper<sup>4‡</sup>, Joerg Heeren<sup>8</sup>, Peter T. C. So<sup>7,9</sup>, Dai Fukumura<sup>4</sup>, Klavs F. Jensen<sup>3</sup>, Rakesh K. Jain<sup>4</sup> and Mounqi G. Bawendi<sup>1\*</sup>

**For *in vivo* imaging, the short-wavelength infrared region (SWIR; 1,000–2,000 nm) provides several advantages over the visible and near-infrared regions: general lack of autofluorescence, low light absorption by blood and tissue, and reduced scattering. However, the lack of versatile and functional SWIR emitters has prevented the general adoption of SWIR imaging by the biomedical research community. Here, we introduce a class of high-quality SWIR-emissive indium-arsenide-based quantum dots that are readily modifiable for various functional imaging applications, and that exhibit narrow and size-tunable emission and a dramatically higher emission quantum yield than previously described SWIR probes. To demonstrate the unprecedented combination of deep penetration, high spatial resolution, multicolour imaging and fast acquisition speed afforded by the SWIR quantum dots, we quantified, in mice, the metabolic turnover rates of lipoproteins in several organs simultaneously and in real time as well as heartbeat and breathing rates in awake and unrestrained animals, and generated detailed three-dimensional quantitative flow maps of the mouse brain vasculature.**

To understand the molecular and cellular mechanisms involved in physiology and disease, biomedical research increasingly aims towards non-invasive imaging with cellular resolution *in vivo*. Fluorescent probes in particular can be detected with very high sensitivity, ultimately allowing the resolution and tracking of single labelled biological entities. This enables the study of rapid biological processes in greater detail than is currently achievable with other imaging modalities, such as magnetic resonance imaging (MRI), ultrasound and computed tomography<sup>1</sup>. However, when imaging whole organisms, there remain several biological obstacles that reduce the sensitivity, acquisition speed and spatial resolution of fluorescence imaging: autofluorescence of tissue or cells adds a background signal, decreasing the contrast and therefore the sensitivity; absorption and scattering of the excitation and emission light by blood and other tissue limits signal detection and impacts acquisition speeds; and scattering limits the spatial resolution as a function of depth, causing blurring of the acquired image.

Imaging in the short-wavelength infrared region (SWIR; 1,000–2,000 nm) addresses all of these challenges simultaneously.

The minimal autofluorescence of biological tissue in the SWIR region leads to increased sensitivity<sup>2,3</sup>, while the significantly reduced light attenuation from scattering and from absorption by the blood and other structures enables imaging with high spatio-temporal resolution and penetration depth<sup>3–9</sup>. Consequently, large organisms such as a whole mouse may be rendered translucent when imaged using SWIR fluorescence<sup>4,8,10</sup>.

Thus far, the lack of a versatile SWIR emitter technology has prevented the general adoption of *in vivo* SWIR imaging, despite its advantages over visible and near-infrared imaging. Versatile probes ideally need to combine a high fluorescence quantum yield (QY) for sensitive and fast imaging, a tunable and narrow emission to generate different colours for multiplexing, and biocompatible functionalizations for specific biological imaging applications.

Here we introduce SWIR-emitting InAs-based core-shell (CS) and core-shell-shell (CSS) quantum dots (QDs) as a versatile class of materials for functional biological imaging (Fig. 1). These InAs-based QDs exhibit a dramatically higher QY and stability than previously described SWIR probes<sup>2,3,8,9,11–17</sup>, as well as a narrow and

<sup>1</sup>Department of Chemistry, Massachusetts Institute of Technology, 77 Massachusetts Avenue, Cambridge, Massachusetts 02139, USA. <sup>2</sup>Department of Materials Science and Engineering, Massachusetts Institute of Technology, 77 Massachusetts Avenue, Cambridge, Massachusetts 02139, USA.

<sup>3</sup>Department of Chemical Engineering, Massachusetts Institute of Technology, 77 Massachusetts Avenue, Cambridge, Massachusetts 02139, USA.

<sup>4</sup>Edwin L. Steele Laboratories for Tumor Biology, Massachusetts General Hospital and Harvard Medical School, 100 Blossom Street, Cox-7, Boston, Massachusetts 02114, USA.

<sup>5</sup>Department of Genetics and Complex Diseases and Sabri Ülker Center, Harvard T.H. Chan School of Public Health, 665 Huntington Avenue, Boston, Massachusetts 02115, USA.

<sup>6</sup>Raytheon Vision Systems, Goleta, California 93117, USA. <sup>7</sup>Department of Biological Engineering, Massachusetts Institute of Technology, Cambridge, Massachusetts 02139, USA.

<sup>8</sup>Department of Biochemistry and Molecular Cell Biology, University Medical Center Hamburg-Eppendorf, Martinistrasse 52, 20246 Hamburg, Germany. <sup>9</sup>Department of Mechanical Engineering, Massachusetts Institute of Technology, Cambridge, Massachusetts 02139, USA.

<sup>10</sup>Present addresses: Neurology Clinic and National Center for Tumor Diseases, University Hospital Heidelberg, and Clinical Cooperation Unit Neuro-Oncology, German Cancer Consortium, German Cancer Research Center, 69120 Heidelberg, Germany (L.R.);

Department of Chemistry, University of Toronto, 80 Saint George Street, Toronto, Ontario M5S 3H6, Canada (M.W.B.W.); Department of Chemistry, Brown University, Providence, Rhode Island 02912, USA (O.C.); Korea Institute of Science and Technology, Seoul 02792, Republic of Korea (G.W.H.);

Centre Hospitalier Universitaire Vaudois, Département de Médecine Interne, CHUV-UNIL, Rue du Bugnon 46, 1011 Lausanne, Switzerland (J.K.).

<sup>11</sup>These authors contributed equally to this work. \*e-mail: obruns@mit.edu; tbischof@mit.edu; mgb@mit.edu

size-tunable emission spectrum comparable to established visible-light emitting QDs<sup>18</sup>. To demonstrate some of the capabilities of this imaging platform, we present three different surface functionalizations (Fig. 1), which we use in specific applications: SWIR QD nanosomes, which are labelled lipoproteins, allow the direct quantification of metabolic processes in real time by non-invasively imaging their transition between brown adipose tissue (BAT), blood and liver. Long-circulating SWIR QD phospholipid micelles enable assessment and quantification of heart rate and respiration of both sedated and awake mice. Using SWIR QD composite particles, we perform angiography in the brain of a mouse, directly identifying arteries and veins. Furthermore, these SWIR QD composite particles enable us to quantify blood flow in the vasculature of the brain by tracking individual composite particles during intravital microscopy, which allows visualization of the dramatic differences between blood flow in healthy vasculature and in vessels at the tumour margin, with sufficient spatial and time resolution to measure flow in individual capillaries. In summary, InAs-based QDs excel compared with commonly employed SWIR probes through improved optical properties and easy functionalization. This class of probes is a promising candidate for use in next-generation functional SWIR imaging applications.

## Results

**Characterization of core-shell and core-shell-shell QDs and their functional surface modifications.** A synthesis scheme based on a continuous injection approach<sup>19</sup> allows us to synthesize large, SWIR-emissive InAs core QDs with improved optical quality and improved thermal stability through slow crystal growth at high temperatures. These InAs cores exhibit a narrow size distribution of  $4.3 \pm 0.4$  nm (10%) and exhibit the zinc blende crystal structure of

the bulk material (Supplementary Fig. 1). We employed these InAs cores as the starting material to be overcoated with shells consisting of higher band-gap materials, to yield various InAs CS (InAs–CdSe and InAs–CdS) and CSS (InAs–CdSe–CdS and InAs–CdSe–ZnSe) QDs with broad absorption and bright, photostable emission (Supplementary Figs 2 and 3, and Supplementary Note 1). The emission of the resulting CS and CSS QDs allow us to cover the entire sensitivity range of modern SWIR cameras from 900 to 1,600 nm (Fig. 2a). Exemplary CSS particles are monodisperse with a size distribution as narrow as 8% (Fig. 2b and Supplementary Fig. 4). As a result of employing this new generation of InAs cores as starting materials, our resulting CS and CSS QDs exhibited improved QYs, especially at longer wavelengths. Supplementary Fig. 5 shows that samples typically exhibited QYs of 10–20% in physiological saline solution and remained as photostable colloidal nanocrystals over several months. With a QY of 30% for our best sample, the QYs of our probes are more than 100 times higher than those of commonly used carbon nanotubes (CNTs; 0.1%; Supplementary Note 2) and roughly 10 times higher than the best performing SWIR-emitting materials previously applied to biological imaging<sup>8,9,11,13–17,20</sup> (Fig. 2c). To transfer the prepared CS and CSS QDs into aqueous media and to demonstrate functional imaging with SWIR QDs, we employed three different surface coatings (Fig. 1). Phospholipid micelles allow long blood circulations times (Supplementary Fig. 6) and thus enable angiography and related applications such as vital sign monitoring<sup>21,22</sup>. QDs incorporated into lipoproteins (SWIR QD nanosomes) enable imaging of the energy metabolism of activated tissues and organs in real time. Lastly, we employed large SWIR QD composite particles that were bright enough for single particle tracking during SWIR intravital microscopy, allowing us to generate large-scale

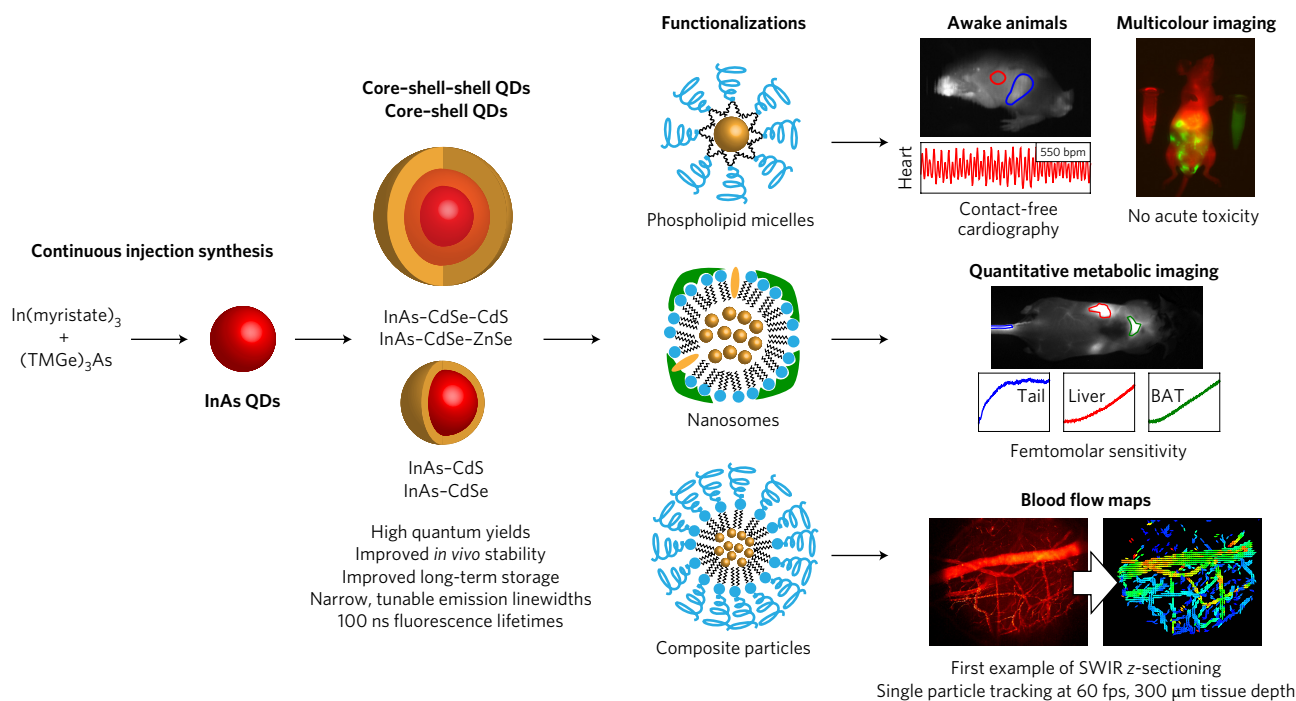


**Figure 1 | Short-wave infrared quantum dots for next generation *in vivo* optical imaging.** A schematic overview of the synthesis of core-shell and core-shell-shell SWIR quantum dots and the subsequent functionalization for next-generation imaging applications is shown. InAs QDs were synthesized via a continuous injection approach, which allows for improved nanocrystal growth over a long time at high reaction temperatures. Subsequently, InAs core QDs were overcoated with various shell materials to allow for a further red-shift and fine-tuning of the emission. The class of synthesized core-shell and core-shell-shell QDs were then functionalized via three distinct surface coatings that tailor the physiological properties for specific SWIR imaging applications. bpm, beats  $\text{min}^{-1}$ .

three-dimensional blood flow maps for a quantitative description of local tissue microenvironments. Figure 2d–f shows that the emission spectra of our probes are only slightly affected by the phase transfer, and high QYs are maintained on phase transfer into physiological buffer. Characterization of size and size-distribution showed small, monodisperse QD phospholipid micelles (21 nm) and larger QD nanosomes (~300 nm) and QD composite particles (~350 nm) with moderate size distributions (Supplementary Fig. 7).

Supplementary Fig. 8 shows that all three surface functionalizations yielded probes with slightly negative zeta potentials. Our library of CS and CSS QDs with narrow emission linewidths and tunable emission readily allowed the acquisition of multiple colours in the SWIR band (Fig. 2g,h and Supplementary Video 1). In addition to a high QY, our CS and CSS QDs exhibited short, excitation-wavelength-independent photoluminescence (PL) lifetimes on the order of 100 ns (Supplementary Fig. 9), which is about one order of

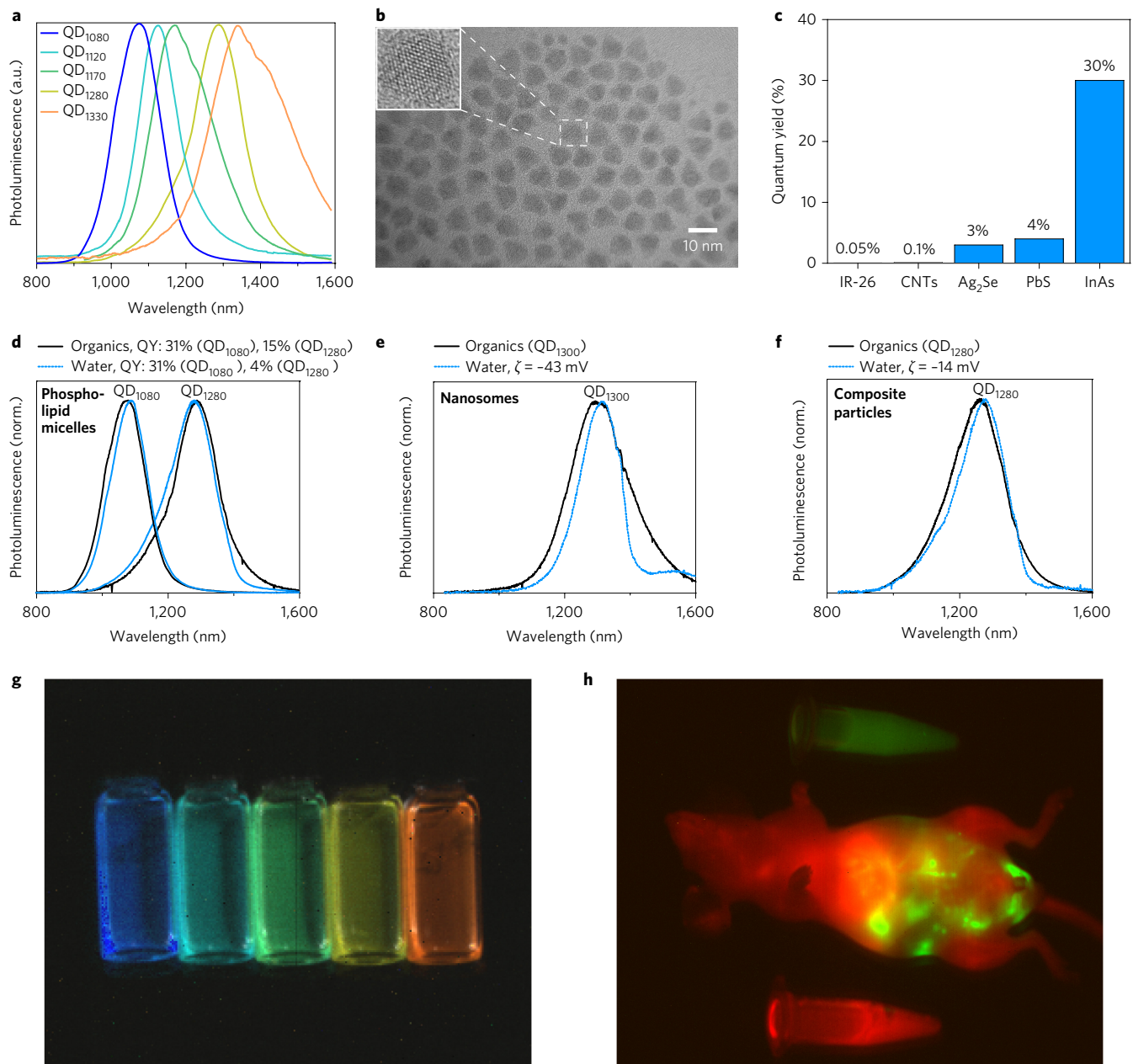


**Figure 2 | InAs core-shell quantum dots with high quantum yield and size-tunable emission for functional and high-speed SWIR imaging.** **a**, Spectra of five different core-shell and core-shell-shell SWIR QDs are shown: QD<sub>1080</sub>, InAs(CdSe)<sub>1</sub>(ZnSe)<sub>3</sub>; QD<sub>1120</sub>, InAs(CdSe)<sub>1.5</sub>; QD<sub>1170</sub>, InAs(CdSe)<sub>3</sub>; QD<sub>1280</sub>, InAs(Cd<sub>0.9</sub>Zn<sub>0.1</sub>S); QD<sub>1330</sub>, InAs(CdSe)<sub>6</sub>. **b**, A representative transmission electron micrograph of CSS SWIR QDs shows monodisperse nanoparticles with a diameter of 7 nm and a narrow size distribution of 8%; inset shows a magnified view of an individual QD. **c**, CS and CSS SWIR QDs exhibited QYs of up to 30% in aqueous buffer, much higher than for previously used materials. **d–f**, The emission spectra remained unaffected after transfer into aqueous buffer from organic solvent for PEGylated SWIR QDs (zeta potential, ζ = -12 mV for QD<sub>1300</sub>) (**d**), nanosomes with SWIR QDs (**e**) and PEGylated SWIR QD composite particles (**f**). Note that water has a very strong absorption band around 1,450 nm, which can be recognized as a feature caused by reabsorption through the solvent in the three spectra. Norm., normalized. **g**, A spectral image of the five samples shown in **a** yielded a pseudo-colour SWIR image. **h**, Two different SWIR QDs were intraperitoneally (green) and intravenously (red) injected into a nude mouse. A spectral image was acquired and separated into red and green by linear unmixing.

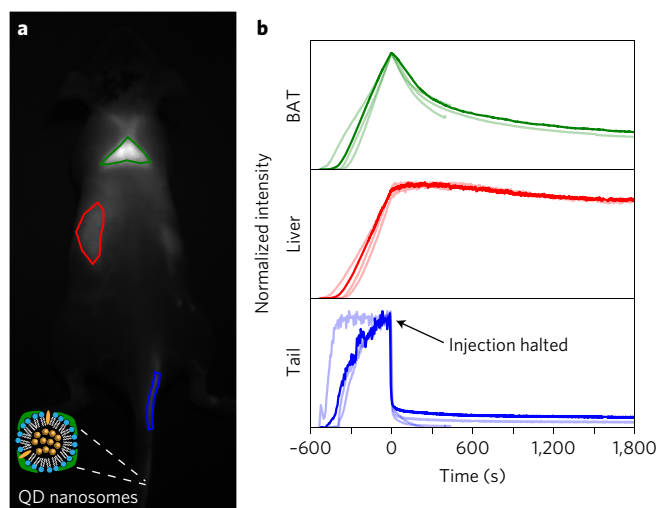


**Figure 3 | QD nanosomes for metabolic imaging.** **a**, A solution of SWIR-QD-labelled recombinant chylomicrons was injected at a constant rate ( $26.7 \mu\text{l min}^{-1}$  or  $0.267 \text{ mg of triglycerides min}^{-1}$ ) into the tail vein of a cold-exposed mouse. The mouse was illuminated using an 808 nm laser at  $15 \text{ mW cm}^{-2}$ , and the SWIR emission was measured for the BAT, liver and tail vein. **b**, This process was repeated for four mice, with the darkened curves representing the results from the mouse shown in **a**, and the lighter curves showing the qualitative similarity of the other mice. The BAT signal after the injection revealed two distinct timescales for clearance: the initial signal loss is consistent with binding and release (time constant,  $\sim 3 \text{ min}$ ; 50% of the signal), while the longer-term component is consistent with uptake (time constant,  $>30 \text{ min}$ ).

magnitude faster than comparable PbS-based QDs. This emission characteristic is important for high-flux applications such as confocal microscopy, as the PL lifetime influences both the maximum excitation flux before saturation is reached and the limit on overall emission output.

**Metabolic imaging with SWIR QD nanosomes.** We and others have recently incorporated visible-light-emitting QDs into lipoproteins to follow their physiologic fate *in vivo*<sup>23–27</sup>. Lipoproteins, in particular triglyceride-rich lipoproteins such as chylomicrons, which are micrometre-size micelles, carry dietary lipids absorbed by the intestine through the lymphatic system into the blood stream and deliver their cargo to peripheral tissues such as brown and white adipose tissue, skeletal muscle and the heart. Similar to glucose, triglyceride-rich lipoproteins are a major source of energy for tissues. Therefore, labelled lipoproteins (SWIR QD nanosomes) allow for a method of studying metabolic activity that is complementary to  $^{18}\text{F}$ -fluorodeoxyglucose positron-emission tomography imaging.

Existing methods, such as MRI and radioactive labelling, are limited by either their sensitivity and dynamic range or their temporal resolution and invasive nature. The relative transparency of tissues at SWIR wavelengths enables tracking of labelled lipoproteins as they circulate and bind to the vasculature of target organs. Additionally, the relative lack of autofluorescence from these tissues enables the detection of low lipoprotein concentrations, and thus allows for quantification within a large dynamic range. BAT is a heat-producing organ, which in response to cold exposure fuels its high metabolic activity by the uptake of triglyceride-rich lipoproteins<sup>24</sup>. To characterize this process, we exposed wild-type mice (four biological replicates) to  $4^\circ\text{C}$  for 24 h to activate their BAT. After sedation and preparation, individual mice were illuminated with an 808 nm source ( $15 \text{ mW cm}^{-2}$ ) and injected with SWIR QD nanosomes (labelled recombinant chylomicrons) via the tail vein at a constant

rate of  $26.7 \mu\text{l min}^{-1}$  for 9.3 min ( $0.267 \text{ mg of triglycerides and } 13.3 \text{ pmol of QDs per minute}$ ; Fig. 3a and Supplementary Video 2). During and after the injection, we imaged the SWIR emission. The time response of the emission intensity arising from BAT, peripheral vasculature and the tail vein (Fig. 3b) was then analysed. The emission intensity in each region of interest (ROI) provided a measure of the relative concentration of the labelled chylomicrons at that location, and halting the injection enabled us to capture the kinetics of the physiological metabolic processes in each organ. The emission intensity for the BAT was detected with subsecond resolution and a noise level of 56 counts. We observed an increase in the emission from BAT at a rate of  $430 \text{ counts s}^{-1}$  during the injection of QDs at  $13.3 \text{ pmol min}^{-1}$  or  $222 \text{ fmol s}^{-1}$ . Therefore, we estimated that the detection sensitivity was  $86 \text{ fmol}$  and the signal-to-noise ratio was 3. This imaging paradigm is robust and technically highly accurate as the biological variation between four replicates could be clearly measured and was not overcome by noise of the measurement (Supplementary Fig. 10). Figure 3b overlays the results to show the reproducibility and biological variation between individual mice.

From these kinetic traces we were able to measure the blood half-life and rate at which chylomicrons are released from the BAT as chylomicron remnants. After the injection into the tail was halted, the particles cleared from the blood and the signal decay for peripheral vasculature was fit well by a sum of two exponential functions and a constant. The blood half-life was on the order of 1 min (values for individual mice:  $73 \pm 1 \text{ s}$ ,  $42 \pm 1 \text{ s}$ ,  $70 \pm 3 \text{ s}$  and  $58 \pm 3 \text{ s}$ ), which is in agreement with previously reported values for cold-exposed mice based on radioactive labelling<sup>24</sup>. The signal from the BAT decayed significantly slower and is fit well by a sum of two exponential functions. The signal remaining in the BAT revealed that initial release of chylomicron remnants, the product of lipolysis, from this tissue occurred with an exponential time constant of  $\sim 3 \text{ min}$  (values for individual mice:  $196 \pm 5 \text{ s}$ ,  $83 \pm 1 \text{ s}$ ,  $195.5 \pm 0.5 \text{ s}$  and  $241.0 \pm 0.5 \text{ s}$ ; roughly half of the bound chylomicrons were cleared in this way). This was followed by a much slower decay on a timescale of  $>30 \text{ min}$  (roughly half of the bound chylomicron population showed this behaviour). The long residence time is consistent with recent reports noting the existence of long-term uptake of particles<sup>24</sup>. The particles released from the BAT and other peripheral tissues were then cleared by the liver.

The SWIR region offers three benefits for this application: first, the longer penetration length allows us to resolve images of organs deep in a mouse; second, as tissues are translucent in this spectral region, small concentrations of SWIR QDs can be detected with high temporal resolution even with a relatively low excitation flux; and third, the relative absence of tissue autofluorescence enables the highly sensitive detection of concentrations down to the femtomolar regime and thus allows quantification over a large dynamic range.

#### High-speed whole body imaging using QD phospholipid micelles.

The high QYs of our QDs, coupled with the fact that tissues are translucent to SWIR, gives rise to high emission signals even under low excitation fluxes. This allowed us to image at acquisition speeds of up to 66.5 frames per second (fps)—limited not by signal but by the readout electronics of our camera—while retaining high resolution and good signal-to-noise at a safe excitation flux. The high QYs allowed an acquisition speed of over twice that reported in previous SWIR imaging studies<sup>11</sup> and at a resolution that was four times greater, resulting in a 10-fold increase in pixel throughput (Supplementary Table 1). Figure 4 and Supplementary Videos 3–5 show whole body imaging of mice, both anaesthetized as well as awake and unrestrained, demonstrating the high speed and high signal-to-background ratio of our SWIR QDs. Indeed, we measured a signal for the heart and liver that is more than two orders of magnitude higher than the background

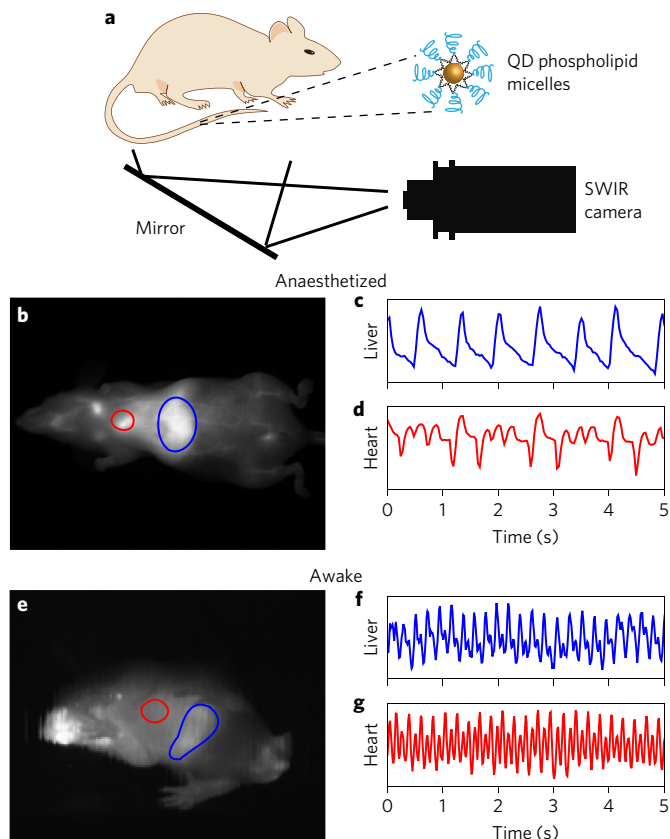


**Figure 4 | High-speed SWIR imaging for contact-free monitoring of heart and respiratory rate in anaesthetized and awake mice using QD phospholipid micelles.** **a,b**, Imaging in the ventral orientation at 30 fps (Supplementary Video 4) with SWIR QDs (808 nm excitation) allowed imaging of vital signs such as heart rate (red ROI in **b**) and respiration (blue ROI in **b**). **c,d**, The respiratory rate of this anaesthetized mouse was 84 breaths  $\text{min}^{-1}$  (**c**) and the heart rate was 130 beats  $\text{min}^{-1}$  (**d**). **e**, The bright emission of our SWIR QDs enabled imaging of an awake mouse (66.5 fps; Supplementary Video 5) and detection of the signal fluctuations generated by motion of the liver and heart. **f,g**, A respiratory rate of 300 breaths  $\text{min}^{-1}$  (**f**) and a heart rate of 550 beats  $\text{min}^{-1}$  (**g**) was observed in this awake but resting mouse.

autofluorescence, and a signal-to-noise ratio for the liver of about 250 or 24 dB for our  $640 \times 512$  pixel camera (Fig. 4b and Supplementary Videos 3 and 4). Both heartbeat and the respiratory cranio-caudal motion of the liver (Fig. 4b and Supplementary Video 4) were clearly resolved. This representative anaesthetized mouse showed a respiratory rate of 84 breaths  $\text{min}^{-1}$  (Fig. 4c) and a heart rate of 130 beats  $\text{min}^{-1}$  (Fig. 4d).

Physiology however, is profoundly affected by anaesthesia. Currently used approaches for measuring the heart rate in awake animals rely on either surgically implanted telemetric sensors or electrocardiography (after confining the animal in a device with conductive pads for recording). The signal emitted by SWIR QDs can overcome this limitation and is in fact strong enough to allow study of freely moving and awake mice, in contrast to most other imaging techniques, such as MRI, computed tomography and ultrasound, which require the mice to be stationary or anaesthetized. We injected long-circulating SWIR QD phospholipid micelles via the tail vein into awake mice and placed them into our imaging setup. After allowing the mice to acclimate, we imaged in the dark, reflecting their usual environment as a nocturnal species. Notably, the 808 nm laser used in this experiment is invisible to mice, as their eyes are even less sensitive to these wavelengths than those of humans<sup>28</sup>.

Figure 4e (Supplementary Video 5) demonstrates our ability to measure the heart and respiratory rates of a mouse, in a contact-free way and without restraining or otherwise affecting the mouse. The recorded heart and respiratory rates of this representative mouse when at rest were 300 breaths  $\text{min}^{-1}$  (Fig. 4f) and 550 beats  $\text{min}^{-1}$  (Fig. 4g), which is in agreement with the literature<sup>29,30</sup> (SWIR QD whole body imaging was reproducibly performed on more than ten mice). *In vivo* SWIR imaging using high-QY QDs thus opens up the possibility of contact-free non-invasive physiological imaging of mice that are awake and undisturbed.

**One-photon excitation SWIR intravital microscopy using SWIR QD composite particles.** The SWIR region of the optical spectrum is also optimal for intravital microscopy. The SWIR region benefits from long wavelength excitation in the near-infrared similar to multiphoton microscopy, allowing deep tissue penetration and relatively high excitation flux without tissue damage. But there is one important difference: multiphoton microscopy relies on two or three photons combining to create a nonlinear excitation event in a fluorophore that then emits in the visible range. This process is seven to eight orders of magnitude less efficient than emission from single photon excitation. The ability to excite in the near-infrared with a one-photon event and detect in the SWIR gives rise to bright emission at moderate excitation intensities (on the order of  $10 \text{ W cm}^{-2}$  in our setup). In comparison, the peak intensity in the focus of multiphoton microscopes is on the order of  $10^6$ – $10^{12} \text{ W cm}^{-2}$ . Additionally, we benefit from the virtual absence of tissue autofluorescence and the high transmission of the SWIR emission. This combination allows us to use an epifluorescence approach to acquire microscopic images at rates and penetration depths that are similar to those of multiphoton microscopy.

We used these benefits of SWIR imaging with QDs to image a glioblastoma multiforme tumour growing in a mouse brain through a transparent cranial window (Fig. 5a). In this experiment, the tumour was pre-labelled by injection of the SWIR QD composite particles three days before imaging. Following pre-labelling, the tumour continued to grow and the long-circulating SWIR QD composite particles were seen to accumulate in collapsed and abnormal tumour blood vessels (Fig. 5b). A second dose of the SWIR QD composite particles was injected and perfusion was imaged at 30 fps across the entire cranial window (Supplementary Video 6). The time series of images was then deconvolved into the pre-labelled tumour (Fig. 5b), the arterial vessels (Fig. 5c) and the venous vessels (Fig. 5d), using a form of principal component analysis<sup>31</sup>. The resulting colour-coded image (Fig. 5e) shows how the growing tumour affected the vascular network.

**Generating quantitative blood flow maps using QD composite particles.** We further demonstrated that SWIR QD composite particles allowed detailed and quantitative imaging of blood flow in relatively large tissue volumes. Quantification of blood flow in the brain is of great importance as it serves as a surrogate for metabolic activity (for example, in functional MRI). Aberrant blood flow in diseases ranging from cancer to stroke often leads to hypoxia. Current approaches to measure blood flow either lack the spatial resolution to resolve individual capillaries (for example, functional MRI) or are too slow to acquire flow information of large volumes (for example, line-scanning multiphoton microscopy<sup>32</sup>).

By imaging the dynamics of the flow in healthy tissue (Supplementary Video 7) and in the tumour margin of a glioblastoma (Supplementary Video 8), *z*-sectioned images of abnormal and normal vasculature in the same mouse were generated (Fig. 6a). The glioblastoma margin showed irregular blood flow, including oscillatory ‘pendular’ flow, while the healthy tissue in the contralateral brain hemisphere showed a normal vessel projection with regular blood flow. Calculating the maximum projection of all frames

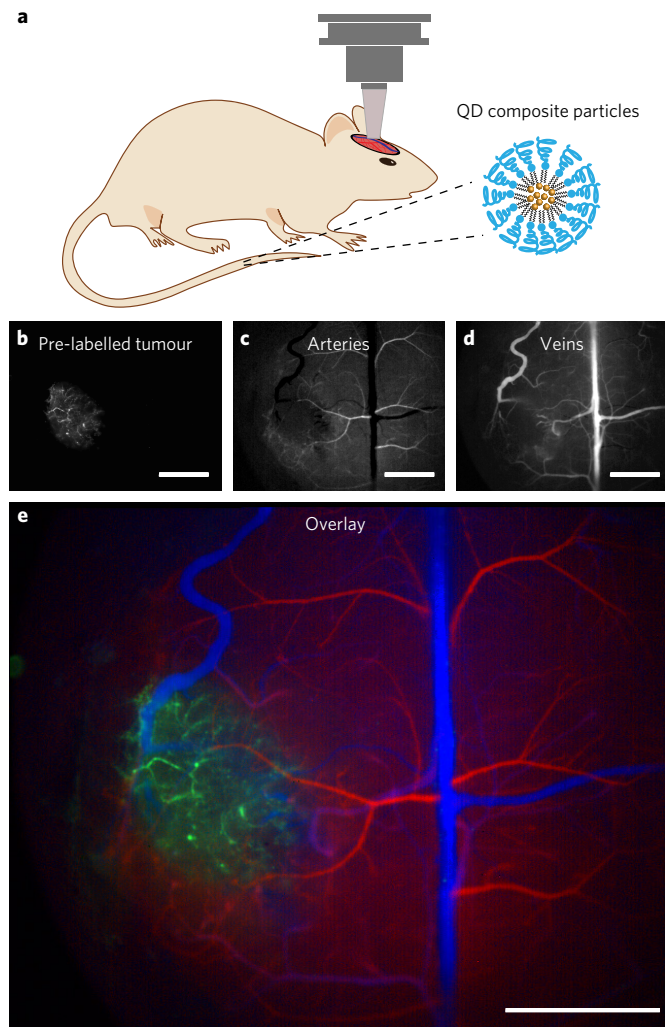


**Figure 5 | High-speed intravital imaging using QD composite particles.** **a,b**, SWIR intravital imaging (808 nm excitation; 1,000 nm longpass for emission) in a mouse with a cranial window (**a**) bearing a glioblastoma multiforme in the left hemisphere of the brain as shown in **b**. **c,d**, Principal component analysis was used to distinguish arteries (**c**) from veins (**d**) in the brain. **e**, This information was colour-coded to create a multicolour angiograph showing the abnormalities of the tumour microvascular network as opposed to normal arterial and venous brain vasculature (green, tumour; red, arterial vessels; blue, venous vessels). Scale bars are 1,500  $\mu\text{m}$ .

allowed visualization of the overall structure of the vasculature in the tumour margin (Fig. 6b) and healthy tissue (Fig. 6c). The details of the vessel structure, however, were confounded by out-of-plane information. Subtracting the average signal of these 600 frames from the maximum intensity projection isolated the signal in the focal plane originating from only individual SWIR QD composite particles (Fig. 6d,e).

In another approach to enhance the contrast of the focal plane and provide true  $z$ -sectioning capability, we calculated the sum of the magnitudes of the difference between each frame's value and the average, which is sensitive only to fluctuations in time, that is, the transit of individual composite particles. The static  $z$ -sectioned images produced in this fashion were comparable to equivalent images produced using multiphoton microscopy. Figure 6f–k directly compares the micrographs of the same fields of view of a healthy mouse brain at various depths, using our  $z$ -sectioning approach (Fig. 6f–h) and conventional multiphoton microscopy (Fig. 6i–k).

We also exploited the unprecedentedly high spatiotemporal resolution of our data to perform particle image velocimetry (PIV)<sup>33–36</sup>, yielding  $z$ -sectioned measurements of the blood flow through the vasculature at 5  $\mu\text{m}$  increments (Supplementary Fig. 11 and Supplementary Video 9). By combining static images of the healthy and tumour-margin vasculature from the areas of the brain shown in Figs 5 and 6 (Fig. 7a,b and Supplementary Videos 7 and 8) with their flow information (Fig. 7c,d), we generated a quantitative representation of blood flow in the tumour margin and healthy brain. This can be extended to a three-dimensional representation of blood flow in the brain as shown for representative healthy mice (Supplementary Fig. 11 and Supplementary Videos 9–12); SWIR QD intravital microscopy with composite particles was performed for different organs in more than ten mice. Each  $z$ -section required 10 s of experimental time (Supplementary Video 10), so that large volumes of brain tissue could be mapped in minutes. The high spatial and velocity resolution of our flow maps arise directly from our ability to accurately measure the motion of individual particles over time, which is only achievable through the use of bright and compact labels, such as our SWIR QD composite particles.

**In vivo safety and toxicological profiles of SWIR QDs.** To examine the safety of SWIR QDs *in vivo*, C57/BL6 mice were administered a single intravenous dose of SWIR QD phospholipid micelles, SWIR QD composite particles or isotonic sodium chloride as a control (seven mice per group). Body weight was measured over the following days and blood and organs were collected six days later to assess acute toxicity. There was no difference in body weight gain between the three groups injected with QD phospholipid micelles, QD composite particles or isotonic sodium chloride. No hepatotoxicity was observed, there being no difference between the three groups for levels of alkaline phosphatase, alanine aminotransferase, aspartate aminotransferase, total bilirubin or albumin. Furthermore, no nephrotoxicity was observed, as there was no difference between the three groups in the levels of blood urea nitrogen, creatinine, calcium, phosphorus, chloride, potassium or sodium. In addition, a complete blood count was performed to identify signs of haematological toxicity. The results showed no differences between the three groups for leukocyte count, red blood cell count, platelet count, haemoglobin levels and haematocrit (Supplementary Table 2).

The SWIR emission from the particles was still present after six days, which indicates that the particles are long-term stable *in vivo* under physiological conditions. Emission from both the QD phospholipid micelles and QD composite particles were exclusively found in the liver and spleen after six days, while other organs such as the lungs, kidneys and the heart showed no emission signal, indicating clearance via liver and spleen. In summary, SWIR QD particles exhibited excellent *in vivo* stability and showed no signs of toxicity six days after injection.

## Discussion

The SWIR spectral range has previously been introduced as a spectral regime where living tissue can become translucent, thus, for example, allowing the observation of brain vasculature through the skin and skull of mice using fluorescence imaging<sup>4</sup>. However, the lack of a versatile SWIR emitter technology has prevented the general adoption of *in vivo* SWIR imaging despite its advantages over visible and near-infrared imaging. Here, we have demonstrated that combining a new generation of high-QY InAs-based CS and CSS SWIR QDs with a class of three surface coatings allows for functional biomedical *in vivo* imaging of both sedated and awake animals, yielding detailed information about metabolism, physiology and pathologic processes, such as tumour angiogenesis.

In one class of applications, the deep penetration of SWIR emission and the low levels of background enable direct measurement of metabolic activity with femtomolar sensitivity in different

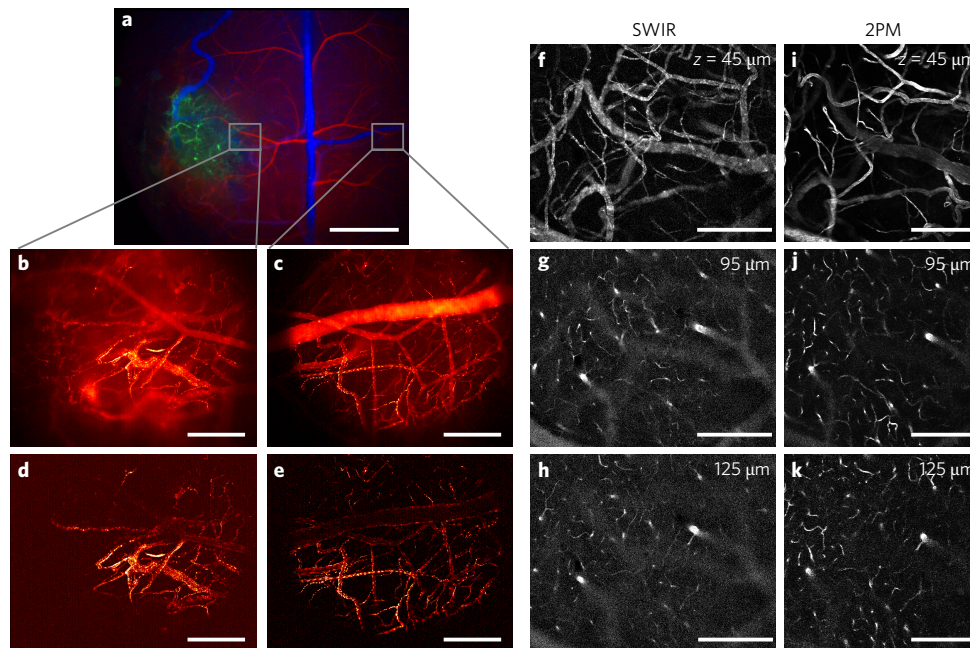


**Figure 6 | High-resolution, high-speed intravital imaging using QD composite particles.** **a–c**, In addition to generating a multicolour angiography image of a glioblastoma tumour through a cranial window (**a**) high-resolution, high-speed QD-SWIR imaging at 60 fps was used to image the vascular network of the tumour margin (**b**) and to compare it to the vasculature in the contralateral hemisphere (**c**). The maximum intensity projections of 600 frames over 10 s are shown in **b** and **c**. By subtracting the average signal of these 600 frames from the maximum intensity projection, the signal originating from only individual QD-SWIR composite particles in the focus was isolated. **d,e**, This enabled isolation of the blood flow in the focal plane, for the tumour margin (**d**) and the vessels on the contralateral lateral side (**e**). To enhance the contrast of the focal plane and provide true z-sectioning capability, we calculated the sum of the magnitude of the difference of each frame from the average, which is sensitive only to fluctuations over time, that is, the transit of individual composite particles. **f–k**, Comparison of micrographs acquired by our z-sectioning approach (**f–h**) with those acquired by conventional two-photon microscopy (2PM) (**i–k**) for the same fields of view of a healthy mouse brain at various depths. Scale bars: **a**, 1,500  $\mu\text{m}$ ; **b–e**, 300  $\mu\text{m}$ ; **f–k**, 200  $\mu\text{m}$ .

mouse tissues by tracking SWIR-QD-labelled lipoproteins. In contrast to existing methods based on radioactive labelling, our technique allows for the measurement of kinetics with a precision (a few seconds) that exceeds the biological variation between mice

of the same group (tens of seconds). With this method, it is now possible to completely measure, in real time and with high dynamic range, lipoprotein processing for several organs simultaneously in individual mice. We anticipate future work in which the individual

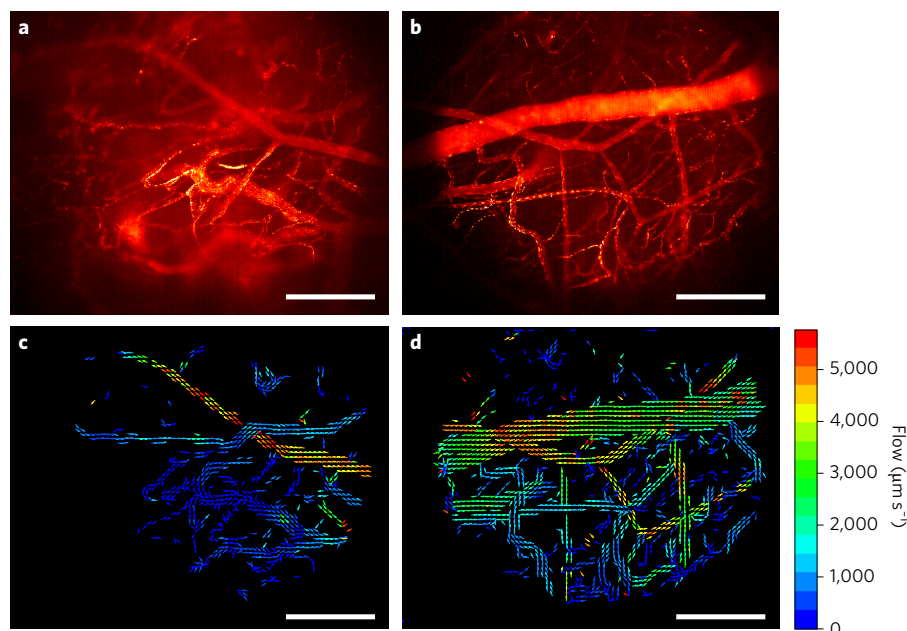


**Figure 7 | High-resolution, high-speed SWIR intravital imaging to generate flow maps of microvascular networks using QD composite particles.** **a–d**, Applying a multi-pass particle image velocimetry approach to the images of the tumour margin (**a**) and healthy hemisphere (**b**) from Fig. 6b,c generated a flow map for each slice (**c** and **d**); coloured arrows indicate the direction and velocity of flow. Scale bars are 300  $\mu\text{m}$ .

mechanisms of binding and uptake can be analysed in greater detail in individual animals, possibly reducing the amount of biological replicates required for quantitative studies. It is also possible to assess the real-time effects of an intervention within an individual animal, such that the results are purely reflective of the effects on the individual and not biased by differences within the population. This approach is not limited to lipoproteins but can be expanded to study the binding kinetics of therapeutic antibodies and other biomolecules.

In a second class of applications, the orders-of-magnitude improvements in signal and long blood circulation lifetimes that QD phospholipid micelles provide, relative to existing SWIR probes, enable imaging of physiological processes that are otherwise too fast to be detected by common imaging methods such as MRI or positron emission tomography. We demonstrated the measurement of the heartbeat and breathing rates in an awake and unrestrained mouse, paving the way for automated and unobtrusive monitoring of animals in their normal environments. This method could be applied to test drug candidates for cardiac arrhythmia, for which SWIR imaging would allow researchers to monitor the animals over time without the need to implant telemetric devices. The ability to non-invasively monitor vital signs would also be beneficial for studies of exercise or behaviour, where it is critical to ensure that the animal is in a normal and unstressed state.

In a third class of applications in a microscopic setting, the strong signal of our QD composite particles enables the measurement of blood flow in the vasculature of the brain. With this method, it is possible to quantify the flow in large volumes of vasculature in only a few minutes of experimental time; for example, before and after an intervention to study ischaemia-reperfusion in stroke. The applications, however, are not limited to pathological processes: almost every tissue can switch between a baseline, resting state and an activated state of enhanced functional performance with increased perfusion; for example, muscle motion, lipolysis of white adipose tissue and heat production by BAT. Similar to functional MRI but with much higher spatial and temporal resolution, our technique of flow measurement may allow quantification and tracking of the activation of certain areas of the brain by detecting changes in blood flow in response to external stimuli.

Central to all of these applications is our ability to appropriately functionalize QDs. Even an emitter with superior optical properties is rendered useless if it cannot be tailored for a given application. The toolkit of SWIR QDs and surface modifications that we present paves the way for widespread adoption of *in vivo* SWIR imaging in the pre-clinical setting. While we did not observe toxic effects in mice during our short-term studies, we realize that the chemical composition of our SWIR QDs probably prohibit their use in humans. Thus, the development of heavy metal-free, high-quality SWIR emitters will be the next challenge in order to bring SWIR imaging into clinical settings. In the meantime, our versatile functional SWIR emitter toolkit opens an avenue towards the broader application of SWIR imaging in biomedical research.

## Methods

**Synthesis of InAs core-shell QDs.** To synthesize QD samples that span the entire SWIR region both the size- and composition-tunability of InAs-based QDs was exploited.

In general, the InAs core sets the initial wavelength and our synthetic approach allows us to synthesize cores with emission wavelengths of ~700–1,200 nm. To access emission wavelengths >1,200 nm, InAs cores were overcoated with either CdSe or CdZnS. In some cases these core-shell QDs were enclosed with an outer shell consisting of a higher band-gap material such as ZnSe or CdS.

**Synthesis of InAs cores.** In a typical procedure, 4 mmol of indium (III) acetate, 14 mmol of myristic acid and 20 ml of 1-octadecene were added to a 50 ml four-neck round bottom flask. The flask was heated to 110 °C under vacuum (10 mtorr) for 2 h to remove acetic acid and form a solution of indium (III) myristate. The indium myristate solution was heated under argon to 295 °C.

An injection syringe containing 0.22 mmol of tris(trimethylgermyl)arsine ((TMGe)<sub>3</sub>As) dissolved in 4 ml of tri-*n*-octylphosphine was prepared in a nitrogen glovebox and rapidly injected into the indium myristate solution at 295 °C. After 10 min, a syringe containing 0.72 mmol tris(trimethylgermyl)arsine dissolved in 1 ml tri-*n*-octylphosphine and 4 ml 1-octadecene was loaded into a syringe pump and the arsenic precursor solution was injected at 4 ml h<sup>-1</sup> at a temperature of 295 °C. The QD size was monitored during this step by removing aliquots from the solution. When the QDs reached the desired size, the precursor injection was stopped and the reaction was removed from the heat source.

The QDs were isolated by filtering the growth solution, diluted in toluene, through a 200 nm polytetrafluoroethylene filter, followed by addition of acetone to cause precipitation of the QDs and then finally centrifugation. The QDs were dissolved in 20 ml of hexane and stored for overcoating. See Supplementary Fig. 1 for the results of the characterization of the InAs QDs.

**Overcoating InAs QDs.** InAs–CdSe–ZnSe QDs were prepared as follows, using a ZnSe overcoating procedure that was adapted from a previously published method<sup>37</sup>. InAs cores (44 nmol) in hexane were added to 4 ml of 1-octadecene, 3 ml of oleylamine and 0.5 ml of 0.05 M trioctylphosphine selenide in trioctylphosphine (TOPSe). The solution was degassed at 100 °C under vacuum (15 mtorr) for 40 min to remove the hexane, and then heated to 230 °C under argon. Solutions (0.47 ml) of 0.05 M cadmium oleate and 0.05 M TOPSe were injected side by side using a syringe pump at 1 ml h<sup>-1</sup> at 230 °C. Then 0.6 ml of 0.05 M diethylzinc was added and the temperature was raised to 250 °C. After 15 min, 0.6 ml of 0.05 M TOPSe was added. After 15 min, 0.75 ml of 0.05 M diethylzinc was added. After 10 min, 0.95 ml of 0.04 M Se dissolved in 1-octadecene (ODE) was added. After 15 min, 1 ml of oleic acid was injected. After 13 min, 0.95 ml of diethylzinc was added. After another 13 min, 1.2 ml of 0.04 M ODE–Se was added. The temperature was raised to 290 °C for 25 min and then the reaction mixture was cooled. The QY was found to be 30% using an integrating sphere. The PL peak was around 1,075 nm.

The preparation of InAs–CdS QDs was adapted from procedures and conditions previously used to make CdSe–CdS core-shell QDs<sup>38</sup>. InAs cores (90 nmol) in hexane were added to 10 ml of ODE. The solution was degassed under vacuum at 100 °C to remove the hexane. At a temperature of 230 °C, 8.2 ml of 0.05 M solutions of cadmium oleate and sulfur in ODE were added side by side using a syringe pump at 5 ml h<sup>-1</sup>. The PL peak was found to be 1,150 nm, with a QY of 35% in chloroform.

InAs–CdSe QDs were prepared by overcoating InAs with CdSe, using a method adapted from a previous publication<sup>20</sup>. InAs cores of 4.95 nm in diameter (30 nmol) in 1 ml of hexane were dissolved in 3 ml of ODE and 2 ml of oleylamine. A vacuum was applied at room temperature to remove the hexane, and then the solution's atmosphere was briefly switched to argon to allow addition of 0.8 ml of 0.05 M TOPSe (about one monolayer worth of Se) in ODE to the reaction. The solution was heated to 100 °C for 1 h under vacuum, before switching to an argon atmosphere and heating to 220 °C. Syringes of 0.045 M of cadmium (II) myristate in trioctylphosphine and 0.05 M TOPSe in ODE were prepared in air, and after the solution reached 220 °C, the cadmium (II) myristate and TOPSe solutions were added to the solution via syringe pump at a rate of 2 ml h<sup>-1</sup>. During the overcoating, the PL peak shifted from 1,080 to 1,420 nm. The large redshift observed here was due to the loss of confinement due to the low conduction-band offset between CdSe and InAs resulting in pseudo-type-II behaviour. After purification by acetone precipitation, the PL peak was blueshifted to 1,380 nm. The QY of the purified solution was measured to be 7% with an emission full-width half maximum of 250 nm. This reaction was designed to add about six monolayers to the InAs cores. Similar procedures were performed to produce particles with bluer wavelengths by using 1.5 and 3 monolayers.

InAs–CdSe–CdS QDs were prepared as previously described<sup>19</sup>. Briefly, purified InAs QDs (96 nmol; diameter of 4.7 nm; PL emission at 1,039 nm) in hexane were transferred to a mixture of ODE (3 ml) and oleylamine (3 ml) in a four-neck flask. The mixture of ODE and oleylamine was previously degassed at 115 °C for at least 1 h. The solution was placed under vacuum to remove the hexane for 30 min at room temperature and another 10 min at 110 °C. Subsequently, the solution was heated to 280 °C for the shell growth. As soon as the mixture reached 240 °C, shell precursor injection was started using 0.05 M shell precursor solutions in ODE. Cadmium oleate (Cd(Ol)<sub>2</sub>; 111 μmol) and TOPSe (111 μmol) were added over the course of 67 min (injection speed, 2 ml h<sup>-1</sup>). InAs–CdSe CS QDs were purified using the above procedure (but using acetone and methanol as non-solvents) and stored in hexane. In contrast to bare InAs cores, the InAs core-shell QDs were not transferred to a glovebox, rather they were stored in air. The size was measured to be 5.1 nm by transmission electron microscopy and the QDs exhibited a PL peak at 1,296 nm. The InAs–CdSe (roughly 86 nmol; 10% loss through aliquots and purification) QDs were then redispersed in ODE (3 ml) and oleylamine (3 ml), and degassed at room temperature for 30 min, and at 100 °C for 10 min. To that solution, 3 ml of 0.05 M Cd(Ol)<sub>2</sub> and 3 ml of a 0.045 M sulfur (both in ODE) were added (150 μmol of Cd and 135 μmol of S) at 240 °C within 1 h. The final QD diameter was determined by transmission electron microscopy to be 6.9 nm with a PL emission peak at 1,307 nm. Elemental analysis using energy-dispersive X-ray spectroscopy indicated the following element ratios: In:As = 1.0 (theoretically 1.0), Cd:(Se + S) = 1.2 (theoretically 1.1), S:Se = 1.9 (theoretically 1.4) and Cd:In = 7.0 (theoretically 3.0).

**Synthesis of PbS–CdS core–shell QDs.** PbS was synthesized with lead oleate as a Pb precursor, hexamethyldisilathiane as a S precursor, and 1-octadecene as a solvent<sup>39</sup>. All the syntheses were performed under an inert atmosphere. Lead oleate was prepared using lead acetate trihydrate and oleic acid at 120 °C, then the lead precursor was heated to 150 °C under nitrogen before injection of the sulphur precursor. After cooling to room temperature, this solution was transferred into a nitrogen-filled glovebox without air exposure. The synthesized PbS QDs were purified three times by adding methanol and 1-butanol until the solution was turbid, followed by centrifugation to precipitate the QDs. The supernatant was discarded and the QDs were re-dissolved in hexane. PbS–CdS core–shell QDs were prepared by cation exchange<sup>40,41</sup> at 100 °C for 5 min under nitrogen using an excess of Cd(OH)<sub>2</sub>. PbS–CdS core–shell QDs were also precipitated with ethanol and re-dissolved three times in hexane to purify and remove unreacted precursors. See Fig. 2 and Supplementary Figs 2–4 for the results of the characterization of the different core–shell and core–shell–shell QDs.

**Phase transfer and surface modification. QD phospholipid micelles.** QDs were transferred into aqueous buffers using a previously reported procedure<sup>21,22</sup>. Briefly, 2 mg (dry weight) of QDs were mixed with 25 mg of 18:1 PEG2000 PE (1,2-dioleoyl-*sn*-glycero-3-phosphoethanolamine-*N*-[methoxy(polyethylene glycol)-2000]) (ammonium salt) (Avanti Polar Lipids, 880130) in chloroform. After brief sonication for 10 s, the solvent was removed under nitrogen flow and 2 ml of isotonic saline or water were added. To completely solubilize the QDs, the aqueous solution was sonicated with a probe sonicator for 5 min. This solution was filtered through a 0.2 µm filter.

**QD nanosomes.** QD-labelled recombinant triglyceride-rich lipoproteins (QD nanosomes) were produced by a previously reported procedure<sup>23,24</sup>. Briefly, physiological lipoprotein extracts from triglyceride-rich lipoproteins were extracted by the method of Folch<sup>42</sup>. To incorporate the QDs into the recombinant lipoproteins, 20 mg of the lipid extract (approximately 80% triglycerides, 10% cholesterol and 10% phospholipids) were dissolved in chloroform and mixed with 1 mg (dry weight) of InAs core–shell nanocrystals. The solvent was removed and triglyceride-rich lipoproteins were formed in 2 ml of PBS buffer or isotonic saline by sonication with a probe sonicator for 10 min. Before intravenous injection, potential aggregates were removed by filtration using a 0.45 µm filter (2 mg of lipid per mouse).

**QD composite particles.** To obtain composite particles with a long circulation time, 2 mg (dry weight) of QDs were mixed with 5 mg of 18:1 PEG2000 PE (1,2-dioleoyl-*sn*-glycero-3-phosphoethanolamine-*N*-[methoxy(polyethylene glycol)-2000]) (ammonium salt) (Avanti Polar Lipids, 880130), 80 mg of soy bean oil and 1.4 mg of phosphatidylcholine in chloroform. After brief sonication for 10 s, the solvent was removed under nitrogen flow and 2 ml of isotonic saline was added. To form an emulsion of composite particles, the aqueous solution was sonicated with a probe sonicator for 10 min. This solution was filtered through a 0.45 µm filter, yielding a solution of particles which were roughly 400 nm in diameter with a broad size distribution. Supplementary Figs 5–8 show the characterization results for the different functionalizations.

**Optical characterization of QDs. Photoluminescence quantum yield.** QY measurements were obtained using an integrating sphere (Labsphere RTC-060-SF). The sample was illuminated using a 785 nm diode laser with an excitation power of 25 mW that was chopped at 210 Hz. The output was collected using a calibrated germanium detector (Newport 818-IR) through a Stanford Research Systems lock-in amplifying system. An 800 nm coloured glass longpass filter was used to block the excitation beam. The sample was placed in a polytetrafluoroethylene-capped quartz cuvette and a solvent blank was used to ensure that the environment inside the integrating sphere was as uniform as possible. The measured photocurrent was adjusted to account for the external quantum efficiency of the detector when calculating the QY. Finally, the measured QY was corrected to account for leakage of the excitation light and the transmittance of the filter.

**Photoluminescence spectroscopy.** For samples with emission peaks between 900 and 1,300 nm, a single-grating spectrometer (Acton SpectraPro 300i) was used in conjunction with a liquid-nitrogen-cooled InGaAs line camera (Princeton Instruments OMA V; 512 pixels × 1 pixels). Samples were excited with a 532 nm diode laser, and emission was collected using a pair of gold-coated off-axis parabolic mirrors.

**Photoluminescence lifetime.** To measure PL dynamics by time-correlated single-photon counting, samples (solutions in glass vials) were excited by a train of 532 nm, 100-ps-duration pulses generated by a laser diode (PicoQuant LDH-P-FA-530B) at a repetition rate of 100 kHz. The considerable waiting time between pulses (10 µs) ensured that the delayed fluorescence—consistent with long-lived ‘trap’ states on the nanocrystals—decayed below the noise floor of the detector (<10<sup>-3</sup> of the peak signal under these conditions). The pump was attenuated to yield roughly 1 nW of average excitation power, with a roughly 20 µm diameter excitation spot at the sample. Under these low-fluence excitation conditions, the PL decay dynamics were independent of excitation intensity. Accordingly, we consider bimolecular recombination channels to be unimportant.

The emission from the nanocrystals was collected and imaged onto an InGaAs–InP single-photon counting avalanche photodiode (Micro Photon Devices S1R-DH-025-C), fitted with a long-pass filter (Chroma Technology, EP900LP) to suppress the scattered photons from the visible pump. The detector was operated asynchronously from the laser source, with a 2 MHz gate frequency and a 90% duty cycle. Using a PicoHarp 300 (time-correlated single-photon counting system; PicoQuant) and version 2.3.0.0 of the associated software, a decay trace histogram was generated by correlating the times of detection events with the proximal trigger from the pump laser. The time resolution, judged from the onset of the response to unfiltered pump scatter, was ~300 ps. This stemmed primarily from the uncertainty in the detector response at the low over-voltages required for low-noise operation. After verifying that no rapid dynamics were observed, 256 ps time bins were used for data collection.

**Animal procedures. Animal model and cell line.** Murine GL261 cells (GL261 WT) were originally provided by the Frederick National Laboratory (National Cancer Institute, Frederick, Maryland, USA). The GL261-GFP-Gluc cell line was generated by transducing GL261 WT cells with a bicistronic lentivirus vector (under the control of the constitutive cytomegalovirus promoter) containing both green fluorescent protein (GFP) and Gaussian-luciferase (GFP-Gluc) genes separated by an internal ribosomal entry site element<sup>43</sup>, provided by the Massachusetts General Hospital vector core. All cells were grown under serum-free conditions using the NeuroCult NS-A proliferation kit (Stemcell Technologies) and maintained in a humidified atmosphere of 5% CO<sub>2</sub> and 95% air at 37 °C. The GL261-GFP-Gluc cells were repeatedly confirmed as mycoplasma-negative via the Mycoalert Plus Mycoplasma Detection Kit (Lonza), and they were authenticated before use by IDEXX laboratories (North Grafton, Massachusetts, USA).

Approximately 200,000 tumour cells were stereotactically implanted into the left striatum of eight- to ten-week-old male C57BL/6 mice (GL261-GFP-Gluc), 2 mm to the left of the sagittal suture, 0.1 mm rostral of bregma and at 2 mm below the brain surface<sup>44,45</sup>. Intravital images were taken through cranial windows.

**Cold exposure to activate brown adipose tissue.** Mice were housed at 22 °C with *ad libitum* access to a standard laboratory chow diet. Cold exposure (4 °C) was performed in single cages for 24 h. We used male 12-week-old C57BL/6 (Charles River Laboratory) wild-type mice, which were fasted for 4 h before the imaging experiment. For *in vivo* imaging to measure metabolic rates, the mice were anaesthetized and SWIR QD-labelled lipoproteins were injected via a tail-vein catheter with a syringe pump (at a rate of 13.3 µl min<sup>-1</sup>).

Animal experiments were conducted in accordance with the approved institutional protocols of Massachusetts General Hospital and the Massachusetts Institute of Technology.

**SWIR imaging apparatus. Macroscopic imaging setup.** For macroscopic imaging from above or below, we used two configurations of a single custom-built setup.

We coupled a 10 W 808 nm laser (Opto Engine MLL-N-808) in a 910-µm-core metal-cladded multimode fibre (Thorlabs MHP910L02). The output from the fibre was passed through a ground-glass plate (Thorlabs DG20-220-MD) to provide uniform illumination over the working area. The excitation flux in this configuration was around 15 mW cm<sup>-2</sup>. The working area comprised a plate of clear glass affixed atop four 1 inch pillars, 6 inch off the table for illumination from above or 12 inch off the table for illumination from below.

We used a 4 inch square first-surface silver mirror (Edmund Optics, 84448) to direct the emitted light through various filters (Thorlabs and Edmund Optics) to a Princeton Instruments Nirvana equipped with various C-mount camera lenses (Navitar). The whole assembly was surrounded by a partial enclosure to eliminate excess light while enabling manipulation of the field of view during operation.

**Microscopic imaging setup.** We used a Nikon Ti-E inverted microscope equipped with a Stage UP Kit (Nikon) and a backport adaptor. For illumination we used a 808 nm laser diode coupled to a fibre which was attached to the backport adaptor. To eliminate laser speckle we used an Optotune speckle remover (Edmund Optics, 88-397). We used a dichroic filter (Thorlabs, DMLP900R) to direct the excitation light to the sample and a 1,000 nm longpass filter (Thorlabs, FELH1000) to select the emission light. Imaging was performed using a 10× or 2× objective (Nikon CFI Plan Apo Lambda). The Nirvana camera was attached to the sideport of the microscope. The camera was cooled to -80 °C for imaging, and the analogue–digital conversion rate was set at 10 MHz with the gain set to high. Different exposure times resulted in different frame rates.

**Metabolic imaging with functionalized SWIR QDs.** The mice were prepared as described above. For the resulting images, we defined regions of interest representing the tail injection site, interscapular BAT and the liver. The total intensity contained within each ROI was determined and used to produce the time series data. A constant background was removed from each time series, based on the intensities of background fluorescence at the beginning of injection.

To fit the signal from the BAT, we identified the time point when the injection was halted, and noted the intensity of the signal from that point to the end of the experiment. We modelled the signal as a sum of three exponential functions,

two of which had positive amplitudes representing loss of signal, and a third with negative amplitude representing residual gain of signal due to the injection.

**Fluorescence angiography.** We used our microscopic imaging setup with the 2× objective to image the brain of a mouse with a cranial window. We recorded a video (30 fps) of the brain during injection of PEGylated QD composite particles, three days after a similar injection to pre-label the tumour. Using this video we applied a form of principal component analysis, using the PoissonNMF ImageJ plugin<sup>46</sup>. This method identifies the extent to which each pixel can be represented as an artery or vein by relating its temporal profile to those of vessels of known identity. Any signal existing before the injection was assigned as the background or the pre-labelled tumour. From this, we removed a laser speckle artefact by a form of flat-field correction where we combined multiple pre-injection images with different fields of view. The colour image in Fig. 5e represents the overlay of pre-injection, artery and vein images.

**Multiphoton microscopy.** A 10 mg ml<sup>-1</sup> solution of fluorescein isothiocyanate–dextran in phosphate buffered saline was prepared for *in vivo* vessel tracing. Following tail-vein injection of 100 µl of this solution, a vessel image was acquired using multiphoton imaging as described previously<sup>48</sup> on a custom-built multiphoton laser-scanning microscope with a confocal laser-scanning microscope body (Olympus 300; Optical Analysis) and a broadband femtosecond laser source (High Performance MaiTai; Spectra-Physics). Image slices were taken with 300 mW at a wavelength of 810 nm. Imaging studies were performed using a 20× magnification, 0.95 numerical-aperture water-immersion objective (Olympus XLUMPlanFl, 1-UB965, Optical Analysis). Image analysis was carried out using ImageJ (National Institutes of Health).

**Particle image velocimetry.** The PIV code was written in Matlab 2015a (MathWorks) and is available at <https://github.com/massivehair/PIV>.

First, the image stack was segmented into two regions, one containing flow and the other containing background. This was achieved by first smoothing every frame in the stack using a Gaussian smoothing kernel with a sigma parameter of two pixels. The standard deviation of each  $x, y$  position in the stack was taken as a measure of the amount of motion in that part of the image. Finally, a greyscale image erosion operation using a disk kernel with a diameter of 25 pixels was used to reduce the influence of noisy pixels and isolated high-variance regions of the image. A threshold could then be selected to distinguish flowing regions from background. Since the effect of this threshold (and the prior steps) is to reduce the computational load of calculating large areas in which there is no flow, the algorithm is not especially sensitive to the choice of smoothing kernel, or whether a threshold is too low; any errors will simply reduce computational efficiency. For the data presented in Fig. 7c,d, respective thresholds of 0.05 and 0.1 were used.

To perform the PIV calculation, first, each frame was smoothed using a 5 × 5 pixel Wiener filter. A window size and maximum step size were defined. In the case of the data presented in Fig. 7, the window size was 8 pixels and the step size was 40 pixels. Flow was calculated at grid locations spaced by the window size, provided these locations contained flow information (as assessed by the threshold previously applied). To calculate flow, two sub-images were taken from consecutive frames. One was taken from the first frame, centred on each grid location, with a size given by the window size. The second was taken from the subsequent frame, centred on the same grid location, with a size equal to the sum of the window size and the maximum step size. A cross-correlation was then performed between the two sub-frames; this is termed the correlation map. This was repeated for every grid location, resulting in  $n - 1$  correlation maps for each, where  $n$  is the number of frames in the stack.

Correlation maps were averaged across all frames, following a previously reported method<sup>47</sup>, and then the peak corresponding to the modal flow vector was located using a three-point Gaussian estimator<sup>48</sup>.

**Code availability.** The code for particle image velocimetry was written in Matlab 2015a and is available at <https://github.com/massivehair/PIV>.

**Data availability.** All raw and processed image data generated in this work, including the representative images provided in the manuscript, are available from the corresponding authors on reasonable request.

Received 26 October 2016; accepted 2 March 2017;  
published 10 April 2017

## References

- De Jong, M., Essers, J. & van Weerden, W. M. Imaging preclinical tumour models: improving translational power. *Nat. Rev. Cancer* **14**, 481–493 (2014).
- Welscher, K. *et al.* A route to brightly fluorescent carbon nanotubes for near-infrared imaging in mice. *Nat. Nanotech.* **4**, 773–780 (2009).
- Yi, H. *et al.* M13 phage-functionalized single-walled carbon nanotubes as nanoprobes for second near-infrared window fluorescence imaging of targeted tumors. *Nano Lett.* **12**, 1176–1183 (2012).
- Hong, G. *et al.* Through-skull fluorescence imaging of the brain in a new near-infrared window. *Nat. Photon.* **8**, 723–730 (2014).
- Ghosh, D. *et al.* Deep, noninvasive imaging and surgical guidance of submillimeter tumors using targeted M13-stabilized single-walled carbon nanotubes. *Proc. Natl Acad. Sci. USA* **111**, 13948–13953 (2014).
- Bardhan, N. M., Ghosh, D. & Belcher, A. M. Carbon nanotubes as *in vivo* bacterial probes. *Nat. Commun.* **5**, 4918 (2014).
- Welscher, K., Sherlock, S. P. & Dai, H. Deep-tissue anatomical imaging of mice using carbon nanotube fluorophores in the second near-infrared window. *Proc. Natl Acad. Sci. USA* **108**, 8943–8948 (2011).
- Hong, G. *et al.* Multifunctional *in vivo* vascular imaging using near-infrared II fluorescence. *Nat. Med.* **18**, 1841–1846 (2012).
- Naczynski, D. J. *et al.* Rare-earth-doped biological composites as *in vivo* shortwave infrared reporters. *Nat. Commun.* **4**, 2199 (2013).
- Lim, Y. T. *et al.* Selection of quantum dot wavelengths for biomedical assays and imaging. *Mol. Imaging* **2**, 50–64 (2003).
- Hong, G. *et al.* Ultrafast fluorescence imaging *in vivo* with conjugated polymer fluorophores in the second near-infrared window. *Nat. Commun.* **5**, 4206 (2014).
- Tsukasaki, Y. *et al.* Short-wavelength infrared emitting multimodal probe for non-invasive visualization of phagocyte cell migration in living mice. *Chem. Commun.* **50**, 14356–14359 (2014).
- Tao, Z. *et al.* Biological imaging using nanoparticles of small organic molecules with fluorescence emission at wavelengths longer than 1000 nm. *Angew. Chem. Int. Ed.* **52**, 13002–13006 (2013).
- Dong, B. *et al.* Facile synthesis of highly photoluminescent Ag<sub>2</sub>Se quantum dots as a new fluorescent probe in the second near-infrared window for *in vivo* imaging. *Chem. Mater.* **25**, 2503–2509 (2013).
- Zhu, C.-N. *et al.* Ag<sub>2</sub>Se quantum dots with tunable emission in the second near-infrared window. *ACS Appl. Mater. Interfaces* **5**, 1186–1189 (2013).
- Zhang, Y. Y. *et al.* Ag<sub>2</sub>S quantum dot: a bright and biocompatible fluorescent nanoprobe in the second near-infrared window. *ACS Nano* **6**, 3695–3702 (2012).
- Tsukasaki, Y. *et al.* Synthesis and optical properties of emission-tunable PbS/CdS core-shell quantum dots for *in vivo* fluorescence imaging in the second near-infrared window. *RSC Adv.* **4**, 41164–41171 (2014).
- Chen, O. *et al.* Compact high-quality CdSe–CdS core-shell nanocrystals with narrow emission linewidths and suppressed blinking. *Nat. Mater.* **12**, 445–451 (2013).
- Franke, D. *et al.* Continuous injection synthesis of indium arsenide quantum dots emissive in the short-wavelength infrared. *Nat. Commun.* **7**, 12749 (2016).
- Zhang, Y. *et al.* Biodistribution, pharmacokinetics and toxicology of Ag<sub>2</sub>S near-infrared quantum dots in mice. *Biomaterials* **34**, 3639–3646 (2013).
- Dubertret, B. *et al.* *In vivo* imaging of quantum dots encapsulated in phospholipid micelles. *Science* **298**, 1759–1762 (2002).
- Stroh, M. *et al.* Quantum dots spectrally distinguish multiple species within the tumor milieu *in vivo*. *Nat. Med.* **11**, 678–682 (2005).
- Bruns, O. T. *et al.* Real-time magnetic resonance imaging and quantification of lipoprotein metabolism *in vivo* using nanocrystals. *Nat. Nanotech.* **4**, 193–201 (2009).
- Bartelt, A. *et al.* Brown adipose tissue activity controls triglyceride clearance. *Nat. Med.* **17**, 200–205 (2011).
- Heeren, J. & Bruns, O. Nanocrystals, a new tool to study lipoprotein metabolism and atherosclerosis. *Curr. Pharm. Biotechnol.* **13**, 365–372 (2012).
- Fay, F. *et al.* Nanocrystal core lipoprotein biomimetics for imaging of lipoproteins and associated diseases. *Curr. Cardiovasc. Imaging Rep.* **6**, 45–54 (2013).
- Jung, C. *et al.* Intraperitoneal injection improves the uptake of nanoparticle-labeled high-density lipoprotein to atherosclerotic plaques compared with intravenous injection: a multimodal imaging study in ApoE knockout mice. *Circ. Cardiovasc. Imaging* **7**, 303–311 (2014).
- Jacobs, G. H., Neitz, J. & Deegan, J. F. Retinal receptors in rodents maximally sensitive to ultraviolet light. *Nature* **353**, 655–656 (1991).
- Foster, H. L., Small, J. D. & Fox, J. G. *The Mouse in Biomedical Research: Normative Biology, Immunology, and Husbandry* (Academic Press, 2006).
- Berndt, A., Leme, A. S., Paigen, B., Shapiro, S. D. & Svenson, K. L. Unrestrained plethysmograph and anesthetized forced oscillation methods of measuring lung function in 29 inbred strains of mice. *Mouse Phenome Database* <http://phenome.jax.org/db/q?rtn=projects/projdet&reqprojid=351> (2010).
- Hillman, E. M. C. & Moore, A. All-optical anatomical co-registration for molecular imaging of small animals using dynamic contrast. *Nat. Photon.* **1**, 526–530 (2007).
- Kamoun, W. S. *et al.* Simultaneous measurement of RBC velocity, flux, hematocrit and shear rate in vascular networks. *Nat. Methods* **7**, 655–660 (2010).
- Adrian, R. J. Twenty years of particle image velocimetry. *Exp. Fluids* **39**, 159–169 (2005).

34. Adrian, R. J. Particle-imaging techniques for experimental fluid mechanics. *Annu. Rev. Fluid Mech.* **23**, 261–304 (1991).
35. Shi, Y., Cheng, J. C., Fox, R. O. & Olsen, M. G. Measurements of turbulence in a microscale multi-inlet vortex nanoprecipitation reactor. *J. Micromech. Microeng.* **23**, 75005 (2013).
36. Schindelin, J. *et al.* Fiji: an open-source platform for biological-image analysis. *Nat. Methods* **9**, 676–682 (2012).
37. Aharoni, A., Mokari, T., Popov, I. & Banin, U. Synthesis of InAs/CdSe/ZnSe core/shell1/shell2 structures with bright and stable near-infrared fluorescence. *J. Am. Chem. Soc.* **128**, 257–264 (2006).
38. Li, J. J. *et al.* Large-scale synthesis of nearly monodisperse CdSe/CdS core/shell nanocrystals using air-stable reagents via successive ion layer adsorption and reaction. *J. Am. Chem. Soc.* **125**, 12567–12575 (2003).
39. Hines, M. A. & Scholes, G. D. Colloidal PbS nanocrystals with size-tunable near-infrared emission: observation of post-synthesis self-narrowing of the particle size distribution. *Adv. Mater.* **15**, 1844–1849 (2003).
40. Pietryga, J. M. *et al.* Utilizing the lability of lead selenide to produce heterostructured nanocrystals with bright, stable infrared emission. *J. Am. Chem. Soc.* **130**, 4879–4885 (2008).
41. Supran, G. J. *et al.* High-performance shortwave-infrared light-emitting devices using core-shell (PbS–CdS) colloidal quantum dots. *Adv. Mater.* **27**, 1437–1442 (2015).
42. Folch, J., Lees, M. & Sloane Stanley, G. H. A simple method for the isolation and purification of total lipides from animal tissues. *J. Biol. Chem.* **226**, 497–509 (1957).
43. Wurdinger, T. *et al.* A secreted luciferase for *ex vivo* monitoring of *in vivo* processes. *Nat. Methods* **5**, 171–173 (2008).
44. Kodack, D. P. *et al.* Combined targeting of HER2 and VEGFR2 for effective treatment of HER2-amplified breast cancer brain metastases. *Proc. Natl Acad. Sci. USA* **109**, E3119–E3127 (2012).
45. Kloepper, J. *et al.* Ang-2/VEGF bispecific antibody reprograms macrophages and resident microglia to anti-tumor phenotype and prolongs glioblastoma survival. *Proc. Natl Acad. Sci. USA* **113**, 4476–4481 (2016).
46. Neher, R. A. *et al.* Blind source separation techniques for the decomposition of multiply labeled fluorescence images. *Biophys. J.* **96**, 3791–3800 (2009).
47. Meinhart, C. D., Wereley, S. T. & Santiago, J. G. A PIV algorithm for estimating time-averaged velocity fields. *J. Fluids Eng.* **122**, 285–289 (2000).
48. Marxen, M., Sullivan, P. E., Loewen, M. R., Ehne, B. J. & Jähne, B. Comparison of Gaussian particle center estimators and the achievable measurement density for particle tracking velocimetry. *Exp. Fluids* **29**, 145–153 (2000).

## Acknowledgements

This work received support from the US National Institutes of Health (NIH) in part through 5-U54-CA151884 (M.G.B.), P01-CA080124 (R.K.J. and D.Fukumura), R35 CA197743, P50 CA165962 and R01-CA126642 (R.K.J.), R01-CA096915 (D.Fukumura), the NIH funded Laser Biomedical Research Center through 4-P41-EB015871-30 (M.G.B.), and the US National Cancer Institute/Federal Share Proton Beam Program Income (R.K.J.); the US National Foundation for Cancer Research (R.K.J.), and the Warsaw Institute for Pancreatic Cancer Research and Massachusetts General Hospital

Executive Committee on Research (D.Fukumura); the US Army Research Office through the Institute for Soldier Nanotechnologies (W911NF-13-D-0001; J.A.C., O.C., H.W., G.W.H. and M.G.B.); the US Department of Defence through DoD W81XWH-10-1-0016 (R.K.J.); and the US National Science Foundation (NSF) through ECCS-1449291 (D.Franke and M.G.B.). This work was supported as part of the Massachusetts Institute of Technology (MIT) Center for Excitonics, an Energy Frontier Research Center funded by the US Department of Energy, Office of Science, Office of Basic Energy Sciences under Award Number DE-SC0001088 (T.S.B. and M.W.B.W.). O.T.B. is supported by an European Molecular Biology Organization long-term fellowship. A.B. is supported by a Deutsche Forschungsgemeinschaft Research Fellowship (BA 4925/1-1). D.Franke is supported by a fellowship of the Evonik Stiftung and fellowship of the Boehringer Ingelheim Fonds. This research was conducted with government support under and awarded by the US Department of Defence, Air Force Office of Scientific Research, National Defence Science and Engineering Graduate Fellowship 32 CFR 168a (J.A.C.). J.H. is supported by a grant from the Fondation Leducq—Triglyceride Metabolism in Obesity and Cardiovascular Disease. L.R. received a Mildred Scheel Fellowship (Deutsche Krebshilfe). D.K.H., D.M.M., I.C. and O.B.A. were supported by NSF GRFP fellowships. J.K. was supported by fellowships from the Deutsche Forschungsgemeinschaft and the SolidarImmun Foundation. C.J.R. and P.T.C.S. acknowledge support from NIH 4-P41-EB015871-30, DP3-DK101024 01, 1-U01-NS090438-01, 1-R01-EY017656 -0, 6A1, 1-R01-HL121386-01A1, the Biosym IRG of Singapore–MIT Alliance Research and Technology Center, the Koch Institute for Integrative Cancer Research Bridge Initiative, Hamamatsu Inc., and the Samsung GRO program. We thank S. Roberge and P. Huang for technical assistance. We also thank QDVision for providing an InAs–CdZnS QD sample (InAs-016) used in this study. We are grateful to Gökhan Hotamisligil for critical discussion and continuing support.

## Author contributions

O.T.B., T.S.B., D.K.H., D.Franke, L.R., A.B., F.B.J., J.A.C., M.W.B.W., O.C., H.W., G.W.H., D.M.M., I.C., O.B.A. and J.K. performed the experiments. O.T.B., T.S.B., Y.S. and C.J.R. analysed the data. O.T.B., T.S.B. and M.G.B. wrote the paper and were assisted by D.Franke, A.B. and R.K.J. J.H., P.T.C.S., D.Fukumura, K.F.J. and R.K.J. provided guidance on the study design. J.H. provided lipid samples. All authors reviewed and edited the manuscript.

## Additional information

**Supplementary information** is available for this paper.

**Reprints and permissions information** is available at [www.nature.com/reprints](http://www.nature.com/reprints).

**Correspondence and requests for materials** should be addressed to O.T.B., T.S.B. and M.G.B.

**How to cite this article:** Bruns, O. T. *et al.* Next-generation *in vivo* optical imaging with short-wave infrared quantum dots. *Nat. Biomed. Eng.* **1**, 0056 (2017).

**Publisher's note:** Springer Nature remains neutral with regard to jurisdictional claims in published maps and institutional affiliations.

## Competing interests

The authors declare no competing financial interests.